Localized Heat Transfer from Firebrands to Surfaces

Elias D. Bearinger[a], Jonathan L. Hodges[b], Fengchang Yang[b], Christian M. Rippe[b] and Brian Y. Lattimer[a*]

[a]Virginia Tech, Mechanical Engineering, 635 Prices Fork Rd, Blacksburg, VA, USA, lattimer@vt.edu

[b]Jensen Hughes, 2020 Kraft Dr, Suite 3020, Blacksburg, VA, USA

*Corresponding author

Highlights:

- High resolution heat flux measurements from firebrands to a surface
- Local heat flux measured 25-80 kW/m^2, 2-3.5 times higher than low resolution methods
- Firebrand geometry, wind speed, and wind orientation affect heat flux level and duration

Abstract:

Firebrands are known to cause spot fires and structure ignition far from the fire front, but there is a limited understanding of the heat transfer from firebrands to surfaces. In this work, high resolution heat flux distributions were measured for single firebrands with different geometries using IR thermography and inverse heat transfer analysis. Localized heat fluxes from a single firebrand were measured to be 25 – 80 kW/m^2, which is 2-3.5 times higher than previous work with heat flux gauges and energy balance methods that spatially average the heat transfer from the firebrand. Firebrand geometry, wind speed, and wind speed orientation relative to the firebrand affect the heat flux magnitude and duration of the exposure.

Keywords: firebrand; heat transfer; surface; ignition

1. Introduction

Wildland fires continue to threaten urban communities due to overgrown vegetation and the increasing number of structures built in the wildland area. In these wildland fires, firebrands are lofted far from the fire front where they ignite vegetation and structures starting spot fires. As a result, significant research has focused on understanding the generation, transport, and ignition processes due to firebrands as described in several reviews [1]–[4]. One area cited in these reviews as needing more attention is a better fundamental understanding of how firebrands ignite combustible materials and vegetation. This requires quantifying conditions for firebrands to ignite fuels, firebrand temperature, and heat transfer from the firebrand to the surface.

Early work to understand the ignition of combustible materials and vegetation by firebrands focused on determining the conditions for firebrands to cause different fuels to ignite. Several researchers have investigated the mass of firebrands required to ignition building construction materials [5], [11], [12], [13] and insulations [14], including the effects of wind. Piles of 2.0-7.0 g of firebrands were required for ignition with wind required to cause flaming ignition. This is similar to what is required to cause smoldering wood to transition to flaming [7]. Other researchers have conducted experiments on the ignition of vegetation beds from cylindrical firebrands [6], [8] and disk shaped firebrands [9], with a lower mass of cylindrical shaped firebrands causing ignition due to more surface contact by the firebrands falling down into the fuel bed. Simulations on the effect of contact resistance between firebrands and a wood surface has also shown that decreasing contact resistance increases the temperature rise of wood [10]. These studies indicate that the likelihood of ignition increases with an increase in the firebrand pile size, fuel type, and geometry of the fuel surface. Also, they highlight the complexity of the heat transfer between the firebrands and the fuel surfaces including surface contact effects.

In order to generate realistic firebrands in the laboratory environment, the shape and size of the firebrands must be considered. Filkov et al. [16] collected firebrands during prescribed burns in the New Jersey Pine Barrens. It was found that the majority of firebrands were bark fragments, with less than 30% of the collected samples being pieces of twigs or branches. To measure the cross-sectional area, the bark firebrands were modeled as rectangles, while firebrands made of twig or branch segments were modeled as cylinders. 80% of the measured firebrands had cross-sectional areas between 50 and 200 mm^2. Manzello et al. [17] burned Korean pine trees in a laboratory environment, using water pans to collect the firebrands. All of the firebrands collected were cylindrical in shape, with an average diameter and length of 5.0 and 34 mm, respectively. These results were similar to burning experiments using Douglas fir trees. These results show that firebrands with both rectangular and cylindrical shapes are important.

Limited measurements have been conducted on the heat transfer from firebrands to a surface. Manzello et al. [11] used an energy balance and the firebrand temperature to estimate the average heat transfer across the firebrand to the surface. For a single glowing cylindrical firebrand, the average heat flux over the firebrand was predicted to be 23 kW/m^2 with 1.3 m/s of wind and 34 kW/m^2 with 2.4 m/s of wind. Water cooled heat flux gauges and thin skin calorimeters with 12 mm diameter sensing surfaces were used to measure heat flux levels from single and piles of firebrands [12]. For single cylindrical firebrands (6.35 – 12.7 mm diameter, 25.4 mm long, 0.1 – 0.6 g mass), the heat fluxes were measured to be 7 – 25 kW/m^2 with no wind. A technique to measure spatial heat transfer from firebrands is being developed using a Nd:YAG laser, a quartz platform, and CMOS camera, but no firebrand measurements have been made [18].

The focus of this paper is to provide high resolution measurements of the heat transfer from a firebrand to a horizontal surface to capture the spatial variation below and around the firebrand. Ignition is a local phenomenon that will depend on the highest heat transfer levels from the firebrand. Since the contact between the firebrand and surface may be variable and the air flow around the firebrand may change its temperature non-uniformly, spatial distributions in the heat transfer from the firebrand to the surface are needed to quantify the highest heat transfer levels to assess ignition potential. In this work, the inverse heat transfer method using IR thermography of a stainless steel plate [19], [20] was used to quantify high resolution heat flux distributions from a single firebrand placed on a horizontal surface. The effects of firebrand geometry, firebrand contact with the surface, wind speed, and firebrand orientation with the wind on the heat flux to the surface were quantified. Localized heat flux measurements were spatially averaged to compare with other measurements in the literature.

2. Experimental Methods

A series of experiments were performed to quantify the spatial and temporal variation in heat flux from a single firebrand to a surface. An inverse heat transfer method using IR thermographs was used to quantify the heat flux from the firebrand to the surface at a resolution of 0.4 mm. A description of the apparatus, firebrands, and inverse heat transfer method is provided below along with the test matrix performed in this study.

2.1 Test Apparatus

The experimental setup to quantify the heat transfer from a single firebrand to a surface is shown in Figure 1. The setup consisted of a thin 304SS stainless steel plate painted black, an IR camera to measure temperature of the underside of the plate (Camera 1), an IR camera to measure the firebrand temperature (Camera 2), and a blower to provide wind. Firebrands were placed on a 0.8 mm thick 304SS plate painted black on both sides with four coats of Rust-Oleum™ high-heat black paint with a measured emissivity of ε = 0.97 [21]. The stainless steel plate was square with each side being 0.61 m long and was supported in each corner by a wooden stand. The wooden stand was 0.92 m tall and sufficiently stable that the plate did not move during the testing.

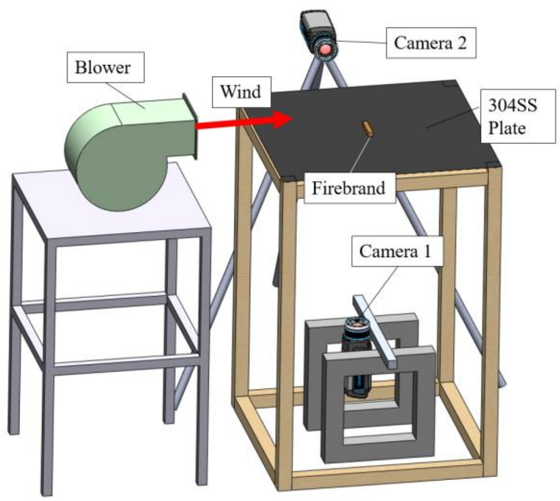

Figure 1. Test stand to characterize localized heat transfer from firebrands.

Two FLIR A655sc infrared cameras operating in the 7-14 μm wavelength range were used to measure surface temperatures. The cameras had a 640 × 480 pixel resolution and used a 24.6 mm (25°) lens. Camera 1 was used to measure the underside of the steel plate and was operated in the 100 – 650°C calibration range. Camera 1 was 0.58 m below the underside of the steel plate resulting in a field of view of the plate of 0.259 m by 0.195 m, which corresponds to a spatial resolution of 0.4 mm. The emissivity for Camera 1 was set to 0.97 to correspond to the black paint emissivity. Camera 2 measured the firebrand surface temperature and was operated using the 300-2000°C calibration range. The distance between Camera 2 and the firebrand ranged from 0.40 – 0.50 m resulting in a spatial resolution of 0.28 – 0.35 mm of temperature on the firebrand. Camera 2 emissivity was set to a value of ε = 0.7 which is the average of the range of emissivity levels (0.6 – 0.8) reported in the literature for firebrands [11], [14], [15]. ResearchIR software was used to control the cameras, collect data, and produce thermal images.

Wind was provided by a Dayton Model No. 1TDR3 Blower (273 cfm @ free air and 60 Hz), connected to a Staco Energy Products Model 3PN151OB Variable Autotransformer to control the wind speed between 0.5 and 2.0 m/s at the firebrand location. Above wind speeds of 2.0 m/s it was found that the firebrands tended to move on the plate. The blower was set up such that bottom of the blower outlet was flush with the top of the plate and the flow traveled parallel to the surface. The bottom of the plate was shielded from the airflow so that there was only natural convection below the plate. The blower was found to be a good laboratory approximation for wind, providing a uniform flow with less than 0.1 m/s variation across the length of the firebrand. Wind speed was verified prior to each test using an Extech Hot Wire Thermo-Anemometer with a 0.2 – 20 m/s range and 0.1 m/s resolution.

2.2 Heat Transfer Measurement

The thermal exposure from firebrands to adjacent surfaces was measured using the inverse heat transfer technique developed by Rippe and Lattimer [20]. The advantage of the inverse heat transfer method is that it measures a heat transfer boundary condition from the firebrand that can then be used to simulate firebrand exposure on a wide variety of surfaces. The technique involves painting a stainless steel plate with a known emissivity paint and exposing one side of the plate to the thermal environment. A series of high resolution IR thermography images of the unexposed side of the stainless steel plate are recorded during testing. An energy balance on each pixel in the IR thermograph is used to calculate the exposure heat flux at every point on the surface using

$$q''_{exp} + q''_{cond} - q''_{rad,b} - q''_{conv,b} = \frac{\rho V c_p}{A}\frac{dT_s}{dt} \quad (1)$$

where q''_{exp} is the exposure heat flux, q''_{cond} is the net lateral heat flux entering a pixel from its neighbors, $q''_{rad,b}$ is the net radiation flux into the unexposed surface, $q''_{conv,b}$ is the net convection flux into the unexposed surface, ρ is the density of the stainless-steel plate, V is the volume of the pixel, A is the surface area of the pixel, c_p is the specific heat of the stainless steel plate, and dT_s/dt is the time rate of change of the surface temperature of the pixel. The exposure flux can be expressed as a heat flux at standard conditions (surface temperature at 293K as would be measured with a Schmidt-Boelter gauge) using the equation

$$q''_{exp} = q''_o - \varepsilon_f \sigma (T_s^4 - T_0^4) - h_f (T_s - T_0) \quad (2)$$

where q''_0 is the heat flux at standard conditions (surface temperature of 293 K), ε_f is the emissivity of the exposed surface, h_f is the convective heat transfer coefficient on the exposed surface, T_s is the measured surface temperature of the stainless steel plate, and T_0 is the standard temperature taken to be 293 K. All heat fluxes presented in this paper are heat fluxes at the standard condition (surface temperature at 293 K).

Rippe and Lattimer showed the uncertainty in the thermal exposure measurements decreased with a larger Δt used in the calculation of the energy storage term in Eq. 1. In this work, Δt of three seconds was used in Eq. 1.

The Nusselt number for natural convection of the heated plate was calculated using the relationships presented by [22] and [23]. For the upper surface of the heated plate,

$$\overline{Nu}_L = 0.54 Ra_L^{1/4} \text{ for } (10^4 \le Ra_L \le 10^7), \quad (3)$$

$$\overline{Nu}_L = 0.15 Ra_L^{1/4} \text{ for } (10^7 \le Ra_L \le 10^{11}) \quad (4)$$

where $\overline{Nu}_L$ is the average Nusslet number, and *Ra* is the Rayleigh number,

$$Ra_L = \frac{g\beta(T_s - T_\infty)L^3}{\nu\alpha} \quad (5)$$

where g is the acceleration due to gravity, β is the thermal expansion coefficient, T_∞ is the ambient air temperature, v is the kinematic viscosity, α is the thermal diffusivity, and L is the hydraulic radius of the heated section

$$L = \frac{A_{exp}}{P_{exp}} \quad (6)$$

where A_{exp} is the total area exposed by the firebrand, and P_{exp} is the total perimeter exposed by the firebrand. Similarly, $\overline{Nu}_L$ for the lower surface of the heated plate,

$$\overline{Nu}_L = 0.27 Ra_L^{1/4} \text{ for } (10^5 \le Ra_L \le 10^{10}). \quad (7)$$

The Nusselt number for forced convection of the heated plate was calculated using the relationships presented by [24] for fully turbulent and laminar boundary layer conditions over a heated flat plate,

$$\overline{Nu}_L = 0.037\, Re_W^{4/5} Pr^{1/3} \text{ for } (Re_W \ge 5 \times 10^5,\ 0.6 \le Pr \le 60) \quad (8)$$

$$\overline{Nu}_L = 0.664\, Re_W^{1/2} Pr^{1/3} \text{ for } (Re_W \le 5 \times 10^5,\ 0.6 \le Pr \le 60) \quad (9)$$

where Re_w is the Reynolds number defined by the plate width, W, and Pr is the Prandtl number.

During preliminary testing, it was observed that the Wiener filter recommended by Rippe and Lattimer to reduce the noise in the thermographs prior to the inverse heat transfer calculation resulted in an increase in noise in this application. In this work, the filter was replaced with a 2-D Gaussian filter with a 7 x 7 pixel window. The updated filtering approach reduced the peak measured temperature by approximately 1 °C, and reduced the peak observed heat flux by 10%.

This series of tests were the first to use the inverse heat transfer (IHT) method in a situation where the thermal response of the stainless steel plate was highly dependent on the spatially resolved conductive flux. Verification of the inverse heat transfer (IHT) method is provided in Figure 2 for a local exposure on a steel plate similar to what would occur in the firebrand testing.

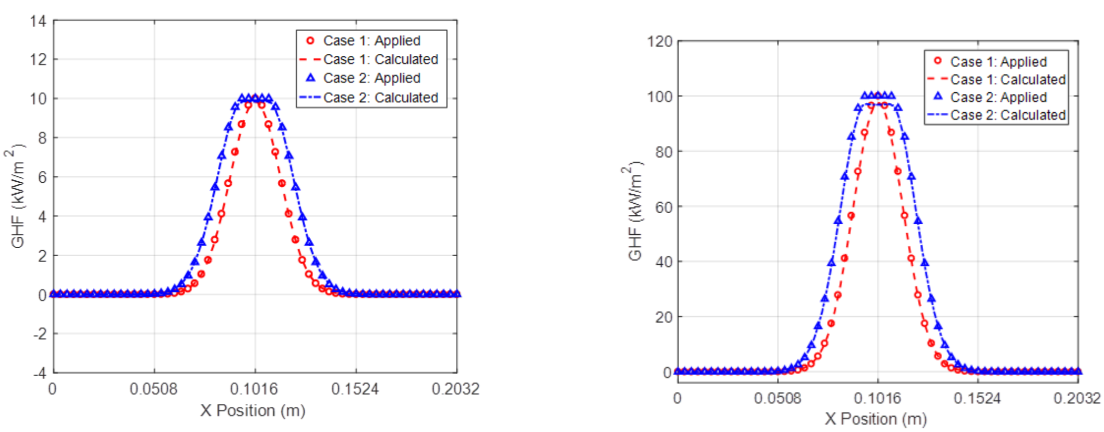

(a) 10 kW/m^2 (b) 100 kW/m^2

Figure 2. Verification for quantifying localized heat transfer using the IHT measurement.

The IHT method was tested by generating artificial thermographs using known exposure profiles in a Finite Element (FE) model in Abaqus. The model included a 0.20 m by 0.18 m plate with continuum heat transfer elements (DC3D8) at a mesh of density of 0.4 mm/element, which was similar to the spatial resolution of the experimental measurements. As seen in Figure 2, two verification scenarios were considered with a local heat flux applied to the center of the plate. Verification Case 1 applied a Gaussian distributed heat flux with a peak value of 10 and 100 kW/m^2 applied at the center with $\sigma = 0.0127$ m in shorter dimension and $\sigma = 0.0254$ m in the longer dimension. Verification Case 2 used the uniform 10 and 100 kW/m^2 heat flux over a 0.025 m x 0.051 m wide rectangle with a Gaussian drop at each edge of the uniform region using the same parameters as Verification Case 1. The error was less than 3%.

2.3 Firebrands

Firebrands were fabricated using oak wood. Six distinct firebrand geometries were manufactured as shown in Figure 3. All firebrands had the same aspect ratio and projected area with the exception of Type 6.

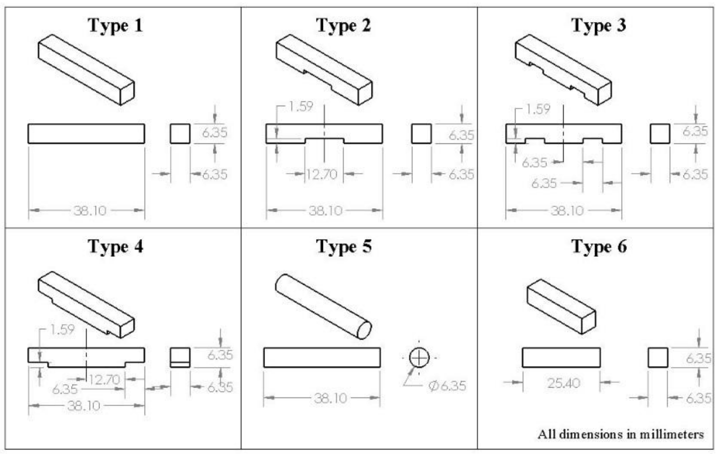

Figure 3. Oak firebrand geometries.

Types 1-4 were all cuboids of the same major dimensions (6.35 mm x 6.35 mm, 38.1 mm long) but with different notches on the face that would be in contact with steel plate surface. The cuboid shape was chosen because it resembles the surface contact of firebrands from bark fragments [16]. The notch depth was 1.59 mm in all cases and spanned the entire width of the firebrand. Type 5 was a cylindrical firebrand (6.35 mm diameter, 38.1 mm long) while Type 6 was a cuboid with no notch and a shorter length (6.35 mm x 6.35 mm, 25.4 mm long). Cylindrical firebrands were selected because they have different surface contact compared with cuboids and they resemble sections of twigs or branches [16], [17]. The cuboid firebrands were manufactured by using a band saw to cut a 38.1 mm x 6.35 mm board into 6.35 mm strips. Notches were installed by hand, using a Dremel rotary cutter. Type 5 firebrands were manufactured by cutting a 6.35 mm round oak dowel into 38.1 mm sections. The moisture content of the firebrands was on average 4.9% by weight with a standard deviation of 0.16%.

Prior to ignition, each firebrand was weighed using an AND HR-202i precision balance with 0.1 mg resolution. The firebrands used for evaluating wind effects were measured using a Sartorius FB6CCE-S scale with a 6200 g range and 0.1 g resolution. To ignite the firebrands, a small propane burner was used. The firebrands were placed in a wire mesh basket over the flames, and rotated frequently to ensure even heating on all sides. Heating over the propane flame lasted for 30s for all firebrands. After the 30s heating period, the flame was turned off and the firebrand was allowed to progress in a state of flaming ignition for an additional 10 s before the flame was blown out. The glowing firebrand was then placed in the center of the stainless steel plate using tongs for testing.

2.4 Test Procedure and Matrix

A matrix of experiments was designed to characterize the effect of wind and wind orientation on the heat transfer from the different types of firebrands. Each firebrand geometry (Types 1-6) was tested under three conditions as outlined in Table 1. This included a no wind condition, wind direction that was parallel to the long-axis of the firebrand, and wind direction perpendicular to the long-axis of the firebrand. Experiments with Type 1 firebrands were run twice to quantify the repeatability.

The majority of testing was performed with a wind speed was 1.0 m/s, with the exception of the Type 2 firebrands (cuboid with one centered notch) oriented perpendicular to the wind where the wind speed was varied from 0 – 2.0 m/s. For all tests, the firebrands were left on the plate for 300 seconds. The initial mass of the wood before creating the firebrand is provided in Table 1 along with the firebrand mass after heating and the mass after the 300 s test. The initial firebrand mass before it was put on the plate was approximately 40-50% of the wood initial mass. Results presented in this paper are based on a single firebrand test for each test condition in the matrix provided in Table 1.

3. Results

Heat transfer measurements from the different types of firebrands are presented in this section for different wind conditions and firebrand orientations relative to the wind direction. In addition, temperature measurements on the long side of the firebrand and repeatability results are provided.

3.1 No Wind

The peak heat flux to the plate with time is provided in Figure 4 for the different types of firebrands tested with no wind. The highest peak heat flux for all firebrands occurred in the initial 25 seconds and then the heat flux decayed with time. Peaks were measured to range from 17-38 kW/m^2 with shorter cuboid (L=25 mm) producing the highest heat flux and the cylindrical cuboid producing the lowest. The cuboidal firebrands were all seen to have similar heat fluxes around 50 s, with variation developing as the test continued. The cylindrical firebrand was measured to have a significantly lower heat flux and decay more rapidly than the cuboids. It was noted during the test that the cuboids progressed in a state of glowing combustion for some time, while the cylinder burned out immediately. The spatial distribution in the heat flux at the time of the highest peak heat flux for the test duration is provided in Figure 5. Except for the cylinder, the heat flux is highest at the distal ends of the firebrands.

Table 1. Firebrand test matrix and mass data.

Type	Description	Wind (m/s)	Wind Orientation	Wood Initial Mass (g)	Mass After Heating (g)	Mass After 300s (g)
1	Cuboid – 6.4 mm x 6.4 mm, 38 mm long	None	N/A	1.221	0.572	0.484
		1.0	Parallel	1.231	0.624	0.386
		1.0	Perpendicular	1.131	0.473	0.238
2	Cuboid – 6.4 mm x 6.4 mm, 38 mm long One centered notch	None	N/A	1.125	0.467	0.357
		None*	N/A	1.1	-	0.3
		0.5*	Perpendicular	1.1	-	0.3
		1.0	Parallel	1.112	0.484	0.331
		1.0	Perpendicular	1.122	0.41	0.208
		1.0*	Perpendicular	1.1	-	0.0
		1.5*	Perpendicular	1.2	-	0.0
		2.1*	Perpendicular	1.1	-	0.0
3	Cuboid – 6.4 mm x 6.4 mm, 38 mm long Two centered notches	None	N/A	1.162	0.55	0.437
		1.0	Parallel	1.128	0.527	0.29
		1.0	Perpendicular	1.092	0.382	0.067
4	Cuboid – 6.4 mm x 6.4 mm, 38 mm long End notches	None	N/A	1.084	0.485	0.405
		1.0	Parallel	1.081	0.512	0.37
		1.0	Perpendicular	1.119	0.495	0.273
5	Cylinder - 6.4 mm diameter, 38 mm long	None	N/A	1.088	0.548	0.524
		1.0	Parallel	1.115	0.554	0.525
		1.0	Perpendicular	1.121	0.551	0.534
6	Cuboid – 6.4 mm x 6.4 mm, 25 mm long	None	N/A	0.81	0.424	0.375
		1.0	Parallel	0.796	0.404	0.326
		1.0	Perpendicular	0.74	0.293	0.158

* Denotes firebrands used to evaluate wind effects.

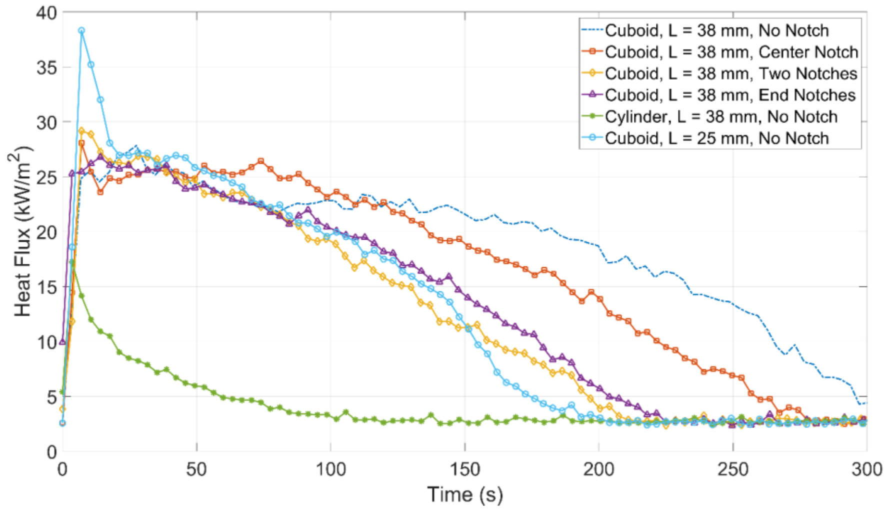

Figure 4. Peak heat flux with time for different types of firebrands with no wind.

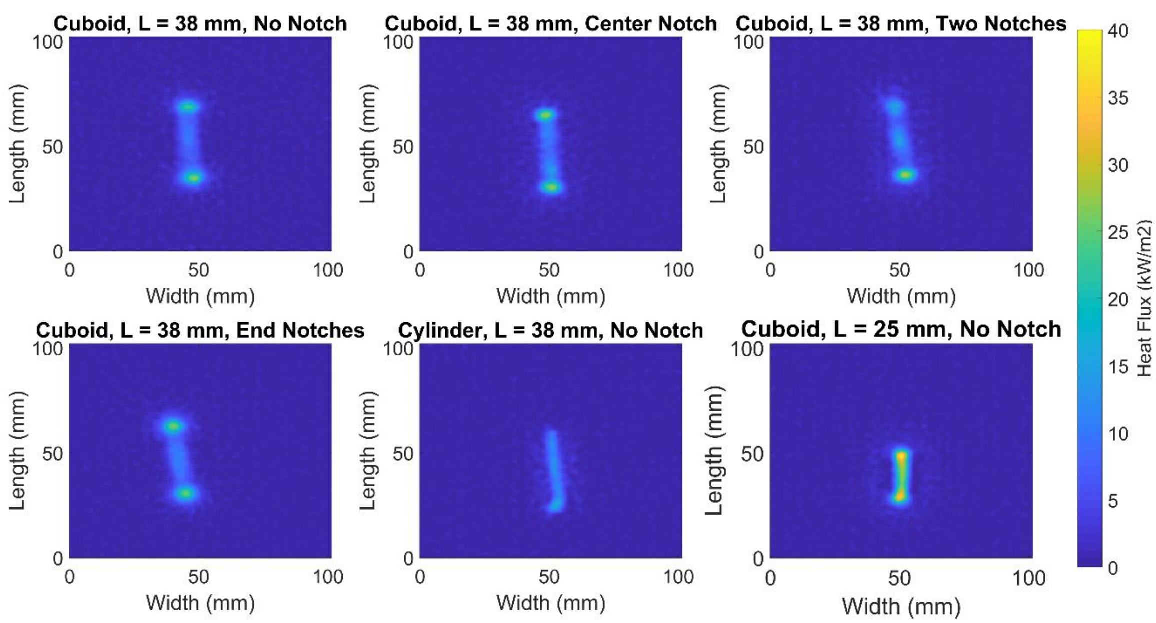

Figure 5. Heat flux distributions at time of highest peak heat flux for different types of firebrands with no wind.

3.2 Parallel Wind

The peak heat flux to the plate with time is provided in Figure 6 for the different types of firebrands tested with the long side parallel to 1.0 m/s of wind. Compared with the no wind case in Figure 4, these heat fluxes are generally higher and remain at an elevated level for a longer period of time. The highest peak heat fluxes ranged from 50-65 kW/m^2 except for the cylindrical firebrand which was significantly lower. For this case, the cuboid firebrand exposure remains above 20 kW/m^2 for 115-300 seconds, depending on the type of firebrand. The cylindrical firebrand produced the lowest heat fluxes and had the shortest duration. The highest heat fluxes were measured to be the cuboid with a single notch. The cuboids, L=38 mm produced similar heat fluxes slightly higher heat fluxes for the case with two center notches. The shorter cuboid, L=25 mm, had a similar heat flux level to the longer cuboids but burned out faster than the longer cuboids.

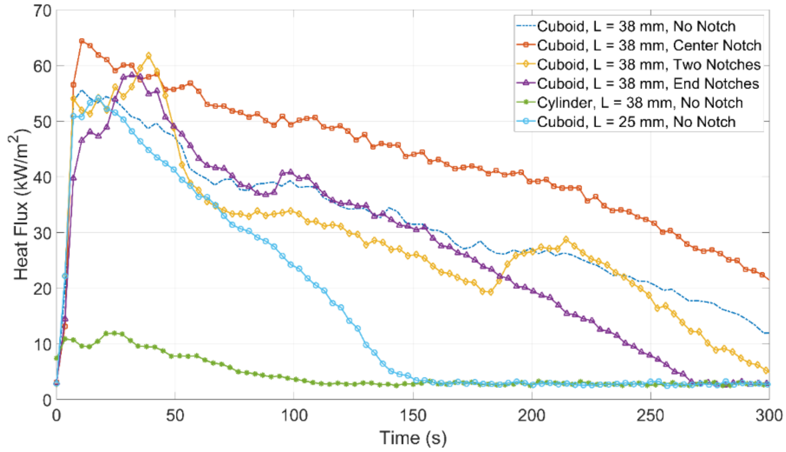

Figure 6. Peak heat flux with time for different firebrands, long side parallel to 1.0 m/s of wind.

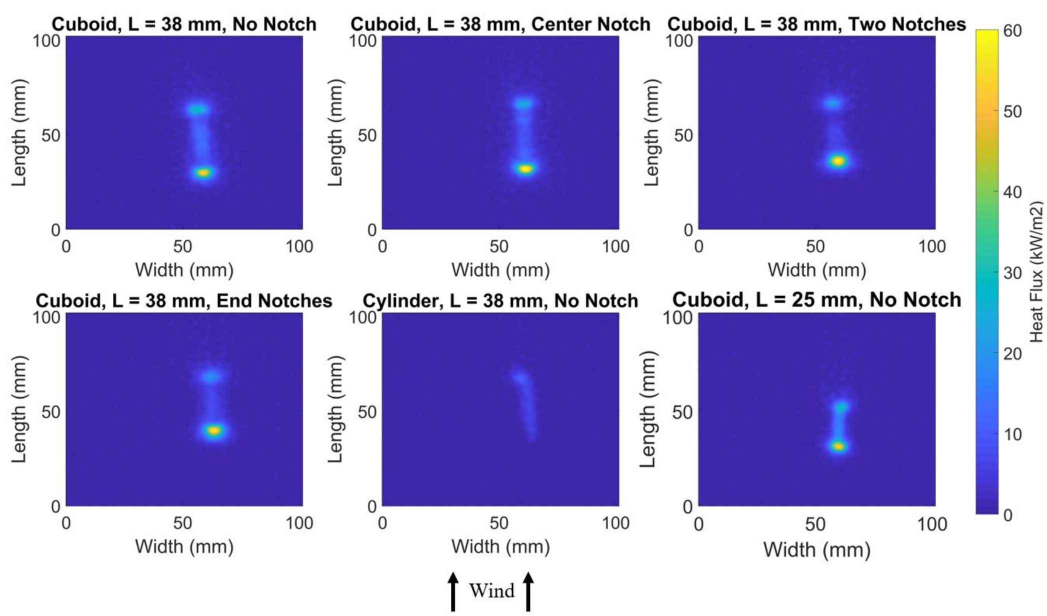

Figure 7. Heat flux distributions at time of highest peak flux for different types of firebrands with long side parallel to 1.0 m/s of wind.

The spatial distribution in heat flux from the firebrands are provided in Figure 7 at the time of the highest peak heat flux. For this case, the highest heat fluxes are generally at the leading edge of the firebrand where the wind initially encounters the firebrand, indicating enhanced char oxidation at the leading edge of the firebrand. The notches in the firebrands are not where the highest heat fluxes were measured, except in the case with the end notches where the leading edge is at the notch location.

3.3 Perpendicular Wind

The peak heat flux to the plate with time is provided in Figure 8 for the different types of firebrands tested with the long side perpendicular to 1.0 m/s of wind. In this case, the highest peak fluxes ranged from 50-75 kW/m^2, excluding the cylindrical firebrand which was again much lower. Exposure of greater than 20 kW/m^2 ranged from 200-300 seconds for all cuboids. The cylindrical firebrand produced the lowest heat flux while the large cuboid without notches generated the highest heat fluxes for most of the test. The peak for the cuboid with two notches corresponds to a sudden, rapid progression of glowing combustion across a substantial portion of the firebrand. In general, these firebrand exposures were similar in duration but slightly higher in magnitude compared with the parallel wind case (Figure 6).

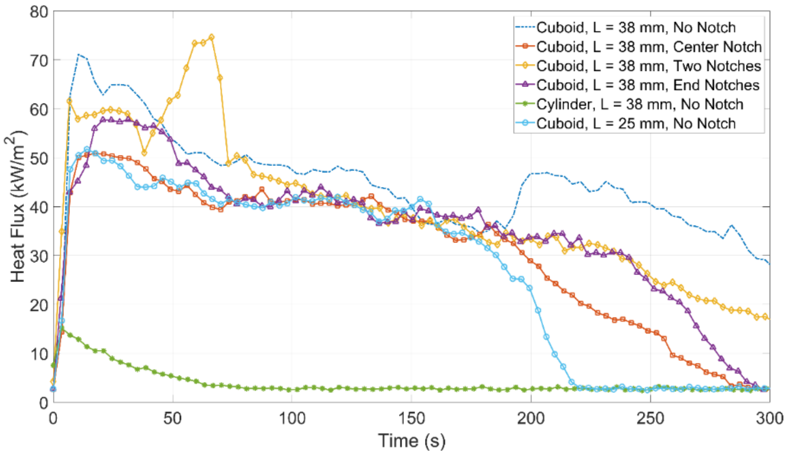

Figure 8. Peak heat flux with time for different types of firebrands with long side perpendicular to 1.0 m/s of wind.

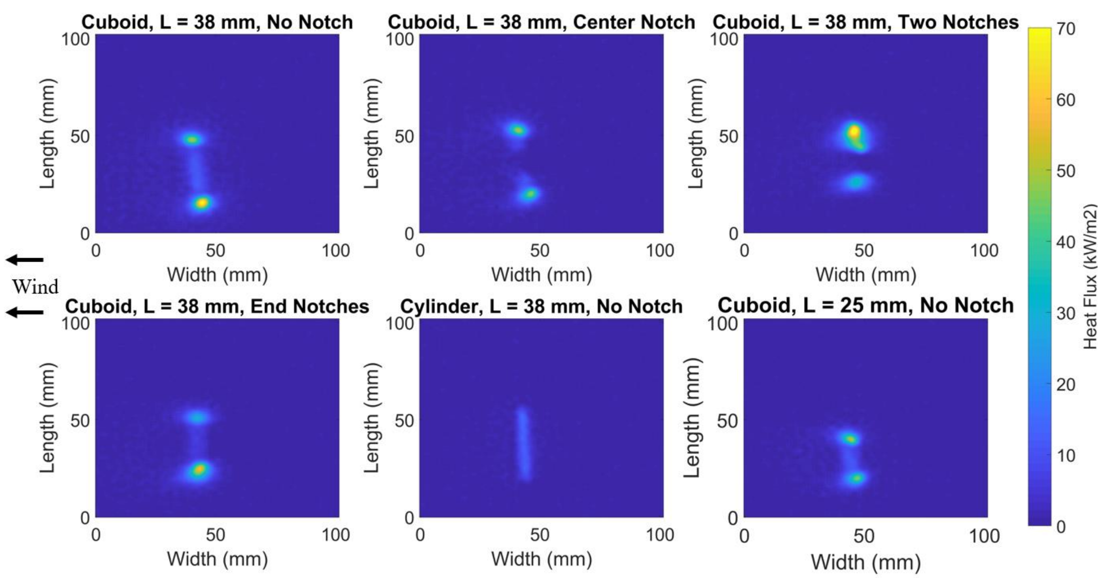

Figure 9. Heat flux distributions at time of highest peak flux for different types of firebrands with long side perpendicular to 1.0 m/s of wind.

Spatial distributions in the firebrand heat flux levels are provided in Figure 9 for the different types of firebrands at the time of the highest peak heat flux level. For this case, the higher heat fluxes are located at the ends of the firebrand, which is attributed to more char oxidation on the ends where there is more surface area.

3.4 Firebrand Temperature

The firebrand temperature distribution at the time of the peak temperature is provided in

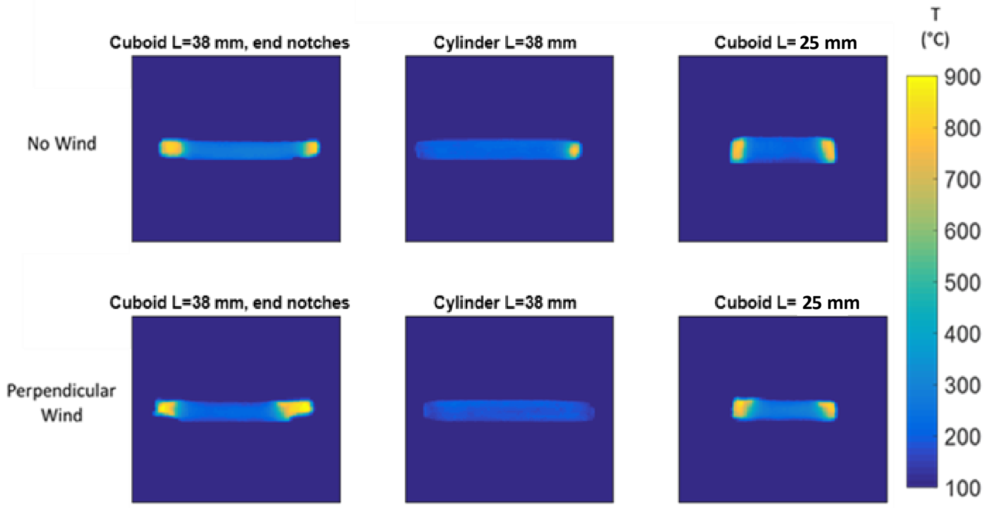

Figure 10. The peak temperatures range from 200-775°C for cylindrical firebrands to 800-950°C for the cuboid firebrands. Highest temperatures were measured at the ends where there is more surface area for char oxidation. The reason why the cylindrical firebrands are consistently lower in temperature compared with the cuboids is unknown. One possible explanation is that all the cuboidal firebrands were cut from a single board, while the cylindrical firebrands were made from a dowel rod. It is possible some variation exists between the two sources which affects the combustion properties of the firebrand.

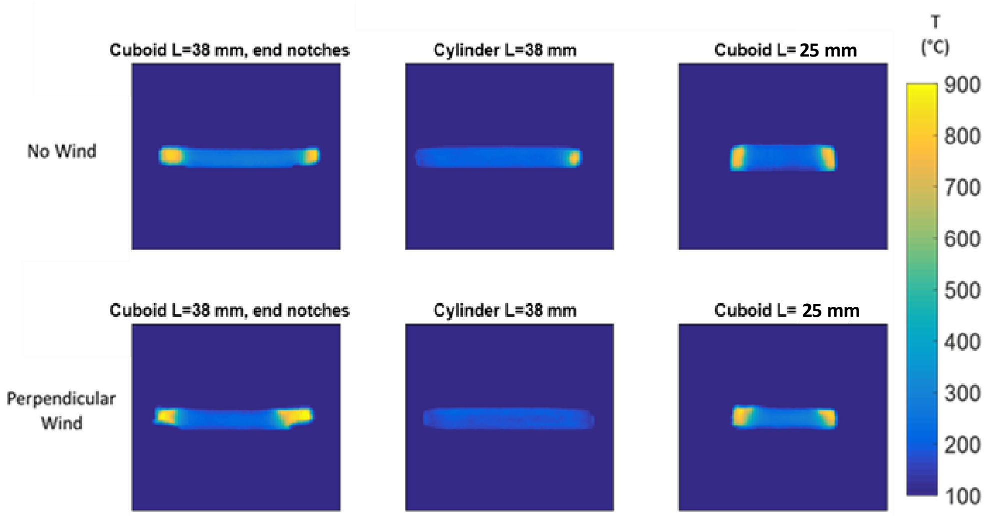

Figure 10. Firebrand temperature distribution at the time of peak temperature for no wind (top row) and firebrand perpendicular to wind at 1.0 m/s (bottom row).

3.5 Wind Speed Effects

The effects of wind speed on firebrand heat flux levels are provided in Figure 11 for a cuboid L=38 mm with a one notch in the center and wind perpendicular to the long side of the firebrand. As expected from previous work, increasing the wind speed causes an increase in heat flux level from 20-30 kW/m^2 with low wind speeds (up to 0.5 m/s) to 50-80 kW/m^2 for wind speeds of 1.0 – 2.0 m/s. In addition, the higher wind speeds caused the firebrands to be consumed faster resulting in intense but shorter duration exposures.

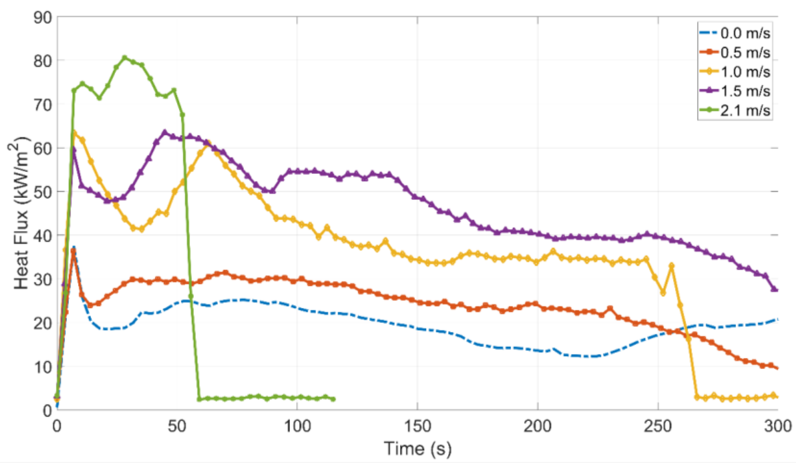

Figure 11. Effect of wind speed on the peak heat flux with time for the cuboid L=38mm, one notch firebrand with the long side perpendicular to the wind.

3.6 Repeatability

Experiments with Type 1 firebrands (6.35 mm x 6.35 mm, 38.1 mm long, with no notch) were run twice to gain an estimate of how consistent the heat transfer was from similar firebrands under the same conditions, shown in Figure 12. Sample A firebrands were used in the rest of the paper, Sample B firebrands were exclusively used for the repeatability analysis. Figure 12 shows peak heat fluxes are similar between tests. The average percent difference between Sample A and B across all three wind conditions was determined to be 5-30% during the primary smoldering period (before 190 s) with a more variation observed as the firebrand smoldering began to decay to burn out (after 190 s).

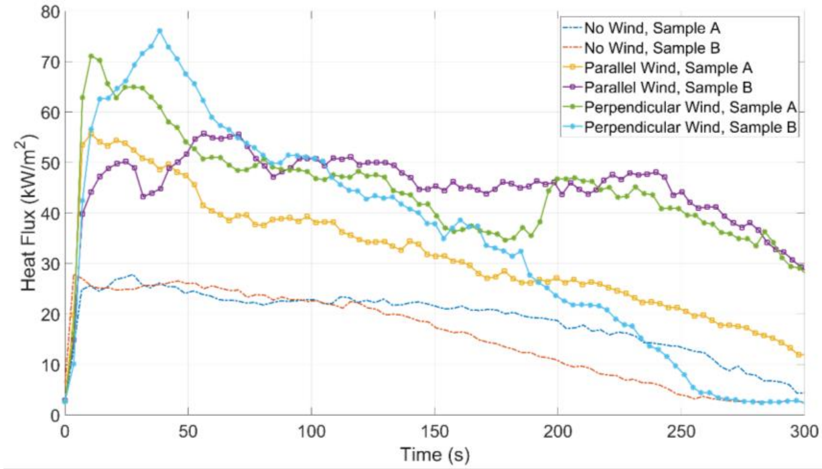

Figure 12. Repeatability of peak heat flux with time (cuboid, L = 38 mm, no notch).

4. Discussion

A summary of the peak heat fluxes measured for the different firebrands in this study is provided in Table 2. In this table, the heat fluxes are provided at three different resolutions: the inverse heat transfer (IHT) method (0.4x0.4 mm resolution), average over firebrand projected area on the surface, and average over a 12.5 mm x 12.5 mm region.

Table 2. Summary of heat fluxes measured in this work at different resolutions.

Description	Wind (m/s)	Wind Orientation	Peak Heat Flux (kW/m^2)		
			IHT Method (0.4x0.4 mm)	Avg. Over Firebrand	12.5x12.5 mm Region Avg.
Cuboid – 38 mm long No Notch	None	N/A	27.8	13.8	9.8
	1.0	Parallel	55.6	17.9	16.1
	1.0	Perpendicular	71.1	21.6	21.2
Cuboid – 38 mm long One centered notch	None	N/A	28.1	13.9	9.9
	None	N/A	37.3	21.7	19.9
	0.5	Perpendicular	36.4	18.8	23.3
	1.0	Parallel	64.4	17.1	17.8
	1.0	Perpendicular	50.9	15.4	14.4
	1.0	Perpendicular	63.3	35.9	31.6
	1.5	Perpendicular	63.4	32.8	32.9
	2.1	Perpendicular	80.6	36.4	40.2
Cuboid – 38 mm long Two centered notches	None	N/A	29.2	12.3	9.5
	1.0	Parallel	61.7	15.8	18.7
	1.0	Perpendicular	74.6	27.3	31.9
Cuboid –	None	N/A	26.8	15.1	9.9

38 mm long End notches	1.0	Parallel	58.3	17.2	18.8
	1.0	Perpendicular	57.8	19.4	21.2
Cylinder - 38 mm long	None	N/A	17.2	11.7	5.8
	1.0	Parallel	11.9	9.9	4.7
	1.0	Perpendicular	15.2	12.3	5.6
Cuboid – 25 mm long	None	N/A	38.3	27.0	12.6
	1.0	Parallel	54.2	25.8	16.0
	1.0	Perpendicular	51.7	21.2	14.5

The firebrand average heat flux was calculated to allow for comparison with heat fluxes predicted using an energy balance on the firebrand [11]. The energy balance prediction of heat flux from a cylindrical firebrand (10 mm in diameter, 75 mm long) was 23 kW/m^2 with a 1.3 m/s wind [11]. This is a 46% difference compared with firebrand average heat flux measured in this study for a cylinder but within 6% of the cuboids. The deviations between the two studies are attributed to the differences in firebrand temperatures.

The 12.5 mm x 12.5 mm average was calculated to compare with measurements using a 12.5 mm diameter heat flux gauge by Hakes et al. [12]. They measured heat fluxes ranging from 7 – 25 kW/m^2 for single cylindrical brands 6.4 – 12.7 mm in diameter and 25 mm long with no wind. This is consistent with the range of 12.5 mm x 12.5 mm average heat flux levels measured in this study shown in Table 2.

The higher resolution heat fluxes are a factor of 2 – 3.5 times higher than the spatially averaged heat fluxes. Some of these heat fluxes are quite localized and the spatial resolution that drives ignition will need to be determined with future experiments of firebrands on combustible materials. Despite this, the technique presented in this paper is able to capture these spatial variations allowing for appropriate averaging to assess the ignition potential of single firebrands and firebrand piles. In addition, the spatial heat flux distributions produced using these measurements also captures the location of the peak heat fluxes which can be uncertain based on the firebrand geometry, contact, and orientation with wind direction.

5. Conclusions

An experimental study was performed to measure the localized heat fluxes produced by different types of single firebrands onto a horizontal surface under different wind conditions. An inverse heat transfer method using a series of IR thermographs of a stainless steel plate provided spatial heat flux distributions with a 0.4 mm resolution. With the higher resolution, peak heat fluxes were measured to be 25 – 80 kW/m^2, which is 2-3.5 times higher than expected based on lower spatial resolutions and values reported in the literature. Firebrand geometry, wind speed and wind orientation relative to the firebrand all affected the peak heat flux produced by the firebrand and the exposure duration. Firebrand experiments on combustible surfaces are needed to determine the appropriate heat flux resolution to correlate with the ignition of the combustible. In addition, work considering multiple firebrands and firebrand piles is necessary to understand how results from single-firebrand experiments scale for more complex systems.

6. Acknowledgements

The project was funded through NIST Grant No. 70NANB19H052.

7. References

[1] S. E. Caton, R. S. P. Hakes, D. J. Gorham, A. Zhou, and M. J. Gollner, "Review of Pathways for Building Fire Spread in the Wildland Urban Interface Part I: Exposure Conditions," *Fire Technol.*, vol. 53, no. 2, pp. 429–473, 2017.

[2] R. S. P. Hakes, S. E. Caton, D. J. Gorham, and M. J. Gollner, "A Review of Pathways for Building Fire Spread in the Wildland Urban Interface Part II: Response of Components and Systems and Mitigation Strategies in the United States," *Fire Technol.*, vol. 53, no. 2, pp. 475–515, 2017.

[3] E. Koo, P. J. Pagni, D. R. Weise, and J. P. Woycheese, "Firebrands and spotting ignition in large-scale fires," *Int. J. Wildl. Fire*, vol. 19, no. 7, pp. 818–843, 2010.

[4] S. L. Manzello, "Enabling the investigation of structure vulnerabilities to wind-Driven firebrand showers in wildland-Urban Interface (WUI) fires," *Fire Saf. Sci. 11*, vol. 11, pp. 83–96, 2014.

[5] V. P. Dowling, "Ignition of timber bridges in bushfires," *Fire Saf. J.*, vol. 22, no. 2, pp. 145–168, 1994.

[6] P. Ellis, "The Aerodynamic and Combustion Characteristics of Eucalypt Bark - A Firebrand Study," *Disseration, Aust. Natl. Univ. Dep. For.*, p. 205, 2000.

[7] T. J. Ohlemiller, "Smoldering combustion propagation on solid wood," *Fire Saf. Sci. 3*, pp. 565–574, 2006.

[8] S. L. Manzello, T. G. Cleary, J. R. Shields, A. Maranghides, W. Mell, and J. C. Yang, "Experimental investigation of firebrands: Generation and ignition of fuel beds," *Fire Saf. J.*, vol. 43, no. 3, pp. 226–233, 2008.

[9] S. L. Manzello, T. G. Cleary, J. R. Shields, and J. C. Yang, "On the ignition of fuel beds by firebrands," *Fire Mater.*, vol. 30, no. 1, pp. 77–87, 2006.

[10] A. Warey, "Influence of thermal contact on heat transfer from glowing firebrands," *Case Stud. Therm. Eng.*, 2018.

[11] S. L. Manzello, S. H. Park, and T. G. Cleary, "Investigation on the ability of glowing firebrands deposited within crevices to ignite common building materials," *Fire Saf. J.*, 2009.

[12] R. S. P. Hakes, H. Salehizadeh, M. J. Weston-dawkes, and M. J. Gollner, "Thermal characterization of firebrand piles," *Fire Saf. J.*, vol. 104, no. June 2018, pp. 34–42, 2019.

[13] S. L. Manzello and S. Suzuki, "Exposing decking assemblies to continuous wind-driven firebrand showers," *Fire Saf. Sci.*, vol. 11, pp. 1339–1352, 2014.

[14] S. S. Wessies, M. K. Chang, K. C. Marr, and O. A. Ezekoye, "Experimental and Analytical Characterization of Firebrand Ignition of Home Insulation Materials," *Fire Technol.*, vol. 55, no. 3, pp. 1027–1056, 2019.

[15] J. L. Urban, A. C. Fernandez-pello, M. Vicariotto, and D. Dunn-Rankin, "Temperature Measurement of Glowing Embers with Color Pyrometry," *Fire Technol.*, vol. 55, no. 3, pp. 1013–1026, 2019.

[16] A. Filkov *et al.*, "Investigation of firebrand production during prescribed fires conducted in a pine forest," *Proc. Combust. Inst.*, 2017.

[17] S. L. Manzello, A. Maranghides, J. R. Shields, W. E. Mell, Y. Hayashi, and D. Nii, "Mass and size distribution of firebrands generated from burning Korean pine (Pinus koraiensis) trees," *Fire Mater.*, 2009.

[18] Y. M. Abul-huda, “Development of a Spatially Resolved Optical Technique for Measuring Heat Flux and Thermal Footprint of Firebrand Piles,” *NIST Tech. Note 2052*, p. 28, 2019.
[19] J. Hodges, C. Rippe, S. W. Case, and B. Y. Lattimer, “Predicting the structural response of a compartment fi re using full-field heat transfer measurements,” *Fire Saf. J.*, vol. 91, no. March, pp. 471–479, 2017.
[20] C. M. Rippe and B. Y. Lattimer, “Full-field surface heat flux measurement using non-intrusive infrared thermography,” *Fire Saf. J.*, vol. 78, pp. 238–250, 2015.
[21] N. Cholewa, P. T. Summers, S. Feih, A. P. Mouritz, B. Y. Lattimer, and S. W. Case, “A Technique for Coupled Thermomechanical Response Measurement Using Infrared Thermography and Digital Image Correlation (TDIC),” *Exp. Mech.*, vol. 56, pp. 145–164, 2016.
[22] R. J. Goldstein, E. M. Sparrow, and D. C. Jones, “Natural convection mass transfer adjacent to horizontal plates,” *Int. J. Heat Mass Transf.*, vol. 16, no. 5, pp. 1025–1035, 1973.
[23] J. R. Lloyd and W. R. Moran, “Natural convection adjacent to horizontal surface of various planforms,” *J. Heat Transfer*, vol. 96, no. 4, pp. 443–447, 1974.
[24] F. P. Incropera, D. P. Dewitt, T. L. Bergman, and A. S. Lavine, *Fundamentals of Heat and Mass Transfer*, 6th ed. Wiley, 2007.